

Geophysical Research Letters®



RESEARCH LETTER

10.1029/2023GL102857

Key Points:

- Trends in seasonal amplitudes of surface ocean pCO₂ are analyzed in observations and CMIP6 simulations with/without anthropogenic forcing
- Applying an Analysis of Covariance, the observed trends in mid-latitude regions are firmly attributed to anthropogenic forcing
- The model ensemble shows large data-model and model-model discrepancies in the pCO₂ seasonal cycle, in particular in high-latitude regions

Supporting Information:

Supporting Information may be found in the online version of this article.

Correspondence to:





F. Joos,
joos@climate.unibe.ch

Citation:

Joos, F., Hameau, A., Frölicher, T. L., & Stephenson, D. B. (2023). Anthropogenic attribution of the increasing seasonal amplitude in surface ocean pCO₂. *Geophysical Research Letters*, 50, e2023GL102857. <https://doi.org/10.1029/2023GL102857>

Received 12 JAN 2023
Accepted 15 JUN 2023

Anthropogenic Attribution of the Increasing Seasonal Amplitude in Surface Ocean pCO₂

Fortunat Joos^{1,2} , Angélique Hameau^{1,2} , Thomas L. Frölicher^{1,2} , and David B. Stephenson³ 

¹Climate and Environmental Physics, Physics Institute, University of Bern, Bern, Switzerland, ²Oeschger Centre for Climate Change Research, University of Bern, Bern, Switzerland, ³Department of Mathematics and Statistics, University of Exeter, Exeter, UK

Abstract A positive trend in time has been noted in the seasonal amplitude of surface ocean pCO₂ over much of the oceans, which is expected to have detrimental impacts on marine ecosystems. To determine whether or not this has an anthropogenic cause, this study investigates historical climate simulations from the Detection and Attribution Model Intercomparison Project with and without anthropogenic forcing. The simulations with anthropogenic forcing show clear evidence of positive trends, whereas the simulations with constant preindustrial atmospheric CO₂ and natural external forcing give only negligible trends. A statistical analysis of five zonal latitudinal bands reveals that the trends detected over 1990–2014 in an ensemble of six observational products are attributable to anthropogenic forcing in mid-latitudes (40°N–10°N, 10°S–40°S), while no trends are detected and modeled in the tropics and the Southern Ocean. Most models fail to represent the sign of the observed climatological mean seasonal cycle difference in high latitudes.

Plain Language Summary Global warming due to fossil fuel use is unequivocal and documented by long records. In contrast, measurements for other important Earth system parameters are only available over recent decades. A short record length makes the attribution of observed trends to human-induced forcing challenging. Trends may be hard to identify due to chaotic Earth system variability. The seasonal amplitude of the partial pressure of CO₂ (pCO₂) in the surface ocean is observed to increase, with global-scale data available since 1990. A continued increase is expected to have negative impacts on fish as the amplified seasonality leads to very high pCO₂, hindering the uptake of oxygen during breathing. Here, we analyze pCO₂ from climate model historical simulations forced by human-caused and natural factors versus simulations with natural factors only. The results allow us to firmly attribute the observed trend in the pCO₂ seasonal amplitude in mid-latitudes to human activities.

1. Introduction

The ocean absorbs around 25%–30% of the current anthropogenic CO₂ emissions (Friedlingstein et al., 2022). This uptake increases the partial pressure of CO₂ (pCO₂) in surface waters and increases the sensitivity of changes in pCO₂ to changes in dissolved inorganic carbon (DIC) and temperature (Broecker et al., 1979; Egleston et al., 2010; Joos et al., 1991; Revelle & Suess, 1957; Zeebe & Wolf-Gladrow, 2001). In turn, the variability of pCO₂ generally increases, with implications for ocean biogeochemical extremes and associated potential impacts on marine organisms and ecosystems (Burger et al., 2020, 2022; Kwiatkowski et al., 2022).

Under future anthropogenic carbon emissions, modeling studies show that the seasonal cycle of pCO₂ and other carbon system variables are not stationary, but rather exhibit strong changes in the seasonal amplitude with increasing DIC (Burger et al., 2020; Fassbender et al., 2018; Gallego et al., 2018; Gorgues et al., 2010; Hauck & Völker, 2015; Kwiatkowski & Orr, 2018; Lerner et al., 2021; McNeil & Sasse, 2016; Rodgers et al., 2008). For example, Gallego et al. (2018) project the seasonal pCO₂ amplitude (SA) in the upper ocean to increase by a factor of 1.5–3 over the next 60–80 years under high carbon dioxide emissions. These authors identify higher DIC, amplifying the seasonal effect of temperature on solubility, as the main driver for the amplification. In high latitudes, the increase in SA is reinforced by decreases in alkalinity due to surface freshening and somewhat damped by reductions in DIC variability (Burger et al., 2020). Similar mechanisms are also projected to enhance the diurnal cycle (Kwiatkowski et al., 2022) and the interannual variability (Gallego et al., 2020) of surface ocean pCO₂. Strong amplifications are also simulated for the seasonal cycle of [H⁺] and associated extreme events (Burger et al., 2020; Kwiatkowski & Orr, 2018). The projected increase in SA may have severe consequences for marine

© 2023 The Authors.

This is an open access article under the terms of the [Creative Commons Attribution-NonCommercial License](https://creativecommons.org/licenses/by-nc/4.0/), which permits use, distribution and reproduction in any medium, provided the original work is properly cited and is not used for commercial purposes.

life and fish catch as it may lead to seasonal hypercapnia, that is, seawater conditions with $p\text{CO}_2 > 1000 \mu\text{atm}$ (McNeil & Sasse, 2016). These model studies focused mainly on results from future projections.

Observations support these model projections. Landschützer et al. (2018) provided observational evidence that *SA* is increasing globally. Interpolating $p\text{CO}_2$ measurements assembled by the Surface Ocean CO_2 Atlas (Bakker et al., 2016), they show that the *SA* increases on average by 2–3 μatm per decade in mid-latitude and high-northern-latitude zonal bands since 1982.

The detection and attribution of observational trends to anthropogenic activities are often not straightforward as natural variability obscures anthropogenic signals (Barnett et al., 2005; Hameau et al., 2019; Hegerl et al., 2010). For example, Keller et al. (2014) find the time of emergence for anthropogenic trends in annual-mean surface $p\text{CO}_2$ to be around a decade, but 45–90 years for sea surface temperature and even longer timescales are identified for anthropogenic deoxygenation (Hameau et al., 2020). It remains therefore unclear whether the observed increase in *SA* over the past few decades can be attributed to human-induced emissions or whether the changes are currently still within the noise of natural internal and externally-forced variability.

This study addresses two main questions:

1. How well are Earth System Models (ESMs) from the Coupled Model Intercomparison Project Phase 6 (CMIP6) able to represent the observed mean state and changes in the $p\text{CO}_2$ seasonality?
2. Can the observed trends in *SA* be attributed to anthropogenic or natural causes?

We analyze *SA* in CMIP6 simulations over the historical period with natural and anthropogenic forcing and simulations with natural forcing only from the Detection and Attribution Model Intercomparison (Gillett et al., 2016, 2021). Using an ANalysis Of COVariance (ANCOVA) regression model, we attempt to attribute observed historical trends in regional mean *SA* to anthropogenic forcing.

2. Data

This study analyses trends in the seasonal cycle amplitude of $p\text{CO}_2$ (*SA*) for each of the 25 years of the common period 1990–2014 in an ensemble of six observation-based global monthly gridded sea surface $p\text{CO}_2$ products (Fay et al., 2021, SeaFlux v2021.04) as well as in 10 simulations from five different ESMs that participated in the sixth phase of the Coupled Model Intercomparison Project (CMIP6) (Eyring et al., 2016). We also discuss climatological mean values of the seasonal cycle difference (SD), given by the difference in $p\text{CO}_2$ between the averages of consecutive winter and summer months (December, January, and February (DJF) and June, July, and August (JJA)). *SA* is defined as the absolute value of SD. For regional averages of *SA*, the $p\text{CO}_2$ data is first averaged regionally and over seasons before evaluating the absolute winter minus summer difference. Three-month periods, used earlier to define *SA* (Landschützer et al., 2018), are selected aiming for a robust comparison between observation-based and simulated *SA*. DJF and JJA are selected to include the observed seasonal extrema of the analyzed latitudinal bands; results are generally similar for JFM minus JAS.

The six observation-based $p\text{CO}_2$ products include three neural-network-derived mappings (CMEMS-FFNN, MPI-SOMFFN, NIES-FNN), a mixed layer scheme product (JENA-MLS), a multiple linear regression (JMA-MLR), and a machine learning ensemble (CSIR-ML6), featuring near-global coverage with a resolution of $1^\circ \times 1^\circ$ for the common period from 1990 to 2019. These products integrate more than 18 million quality-controlled measurements of surface ocean $p\text{CO}_2$ from the Surface Ocean CO_2 Atlas (SOCAT; Bakker et al. (2016)).

The CMIP6 ESM simulations cover the historical period between 1850 and 2014. Two different simulations of each model are used. The first simulations, here briefly termed “HIST,” are driven by a suite of natural (solar, explosive volcanoes) and anthropogenic (greenhouse gases, aerosols, land use) forcing. The “HISTNAT” simulations are run under natural forcing (solar, explosive volcanoes) only, while greenhouse gas concentrations, other radiative forcing agents, and land-use are kept at preindustrial conditions (Gillett et al., 2016, 2021). The focus is on results from five ESMs: ACCESS-ESM1-5 (Ziehn et al., 2020); CESM2 (Danabasoglu et al., 2020); CanESM5 (Swart et al., 2019); IPSL-CM6A-LR (Boucher et al., 2020); NorESM2-LM (Seland et al., 2020). Monthly output of surface ocean $p\text{CO}_2$ is available for both the HIST and HISTNAT simulations for these five models. Part of the analysis is extended to 19 CMIP6 ESMs for which $p\text{CO}_2$ output for the HIST scenario is

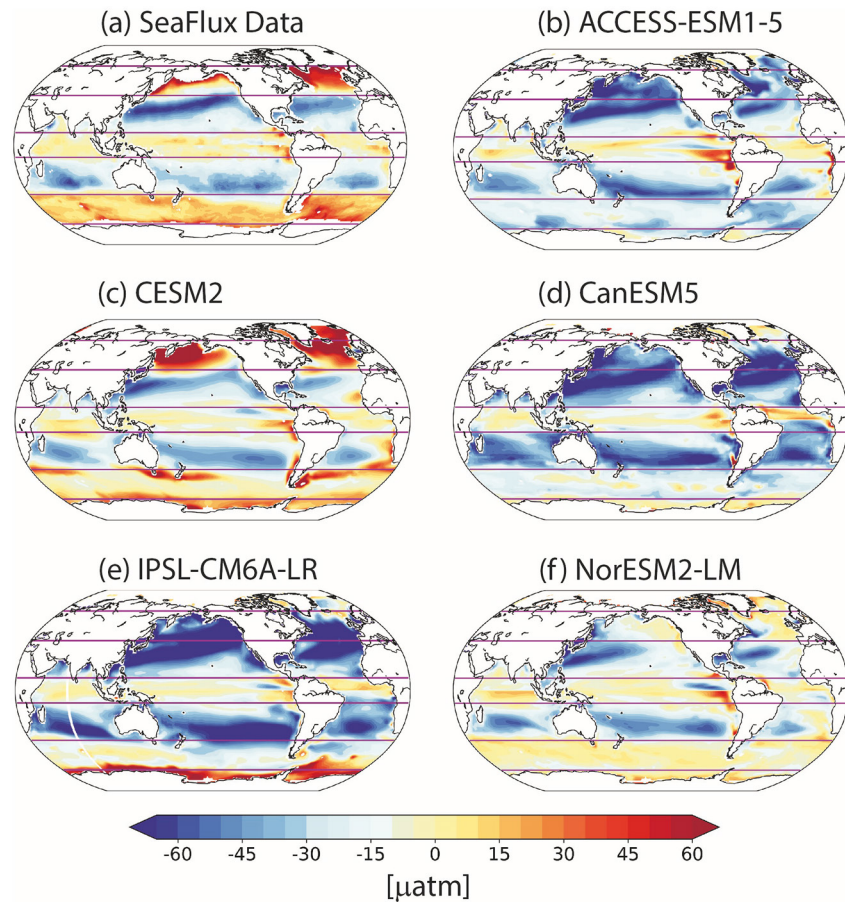


Figure 1. Mean (1990–2014) of the surface ocean $p\text{CO}_2$ seasonal cycle difference for five CMIP6 models running simulation HIST (b–f) compared to the median from six observation-based products (Fay et al., 2021) (a). The seasonal cycle difference is the winter minus the summer mean ((DJF)–(JJA) in the Northern and (JJA)–(DJF) in the Southern Hemisphere). Simulations include combined anthropogenic and natural forcing. Results from additional models are shown in Figures S1 and S3 in Supporting Information S1.

available (see Figures S1–S4 in Supporting Information S1). The monthly output of surface ocean $p\text{CO}_2$ is regridded from the original model grids to a regular ($\approx 1^\circ \times 1^\circ$) grid.

3. Results

3.1. Mean Seasonal Cycle Amplitude of $p\text{CO}_2$

The observation-derived, climatological mean (1990–2014) seasonal cycle difference (winter minus summer) of $p\text{CO}_2$ (SD) shows a latitudinal-dependent, spatial pattern (Figure 1a): a large positive SD poleward of 40°S and 40°N with higher winter than summer $p\text{CO}_2$ and SD locally exceeding $60 \mu\text{atm}$, a reversed seasonal cycle with higher summer than winter values in the subtropical gyre regions and values of SD of up to $\sim -50 \mu\text{atm}$, and a small seasonality in the tropics.

The CMIP6 ESMs (simulations HIST; Figure 1b–f) simulate a small SD in the tropics (multi-model mean \pm sdv = $-0.7 \pm 2.9 \mu\text{atm}$ for 10°N – 10°S ; 1990–2014), in agreement with the observational products ($-1.6 \pm 2.0 \mu\text{atm}$). The negative sign of SD and, broadly, the spatial pattern in SD is captured by the models in the subtropical gyres; larger amplitudes are found toward the poleward edge of the subtropical gyres compared to the boundaries in the tropics. On average, the models overestimate SD compared with the observational products (40°N – 10°N : -33.5 ± 11.5 vs. $-29.9 \pm 2.8 \mu\text{atm}$; 40°S – 10°S : -28.0 ± 8.7 vs. $-22.2 \pm 3.7 \mu\text{atm}$), in particular CanESM5 and IPSL-CM6A-LR. Large differences between simulated and observation-based SD are found in high latitudes (40°N – 65°N : -32.0 ± 34.0 vs. $+28.5 \pm 3.9 \mu\text{atm}$; 40°S – 65°S : -10.2 ± 9.7 vs. $+14.6 \pm 1.4 \mu\text{atm}$).

Only one model (CESM2; Figure 1c) simulates the observed sign of pCO₂ seasonal cycles at high northern latitudes and in the Southern Ocean. NorESM2-LM simulates a very small seasonality in the Southern Ocean. The other three models show in many high-latitude grid cells a reversed seasonality compared to observations. However, the observation-based estimates are uncertain in the Southern Ocean due to the sparsity of winter-time data for this region. Nevertheless, the sign of SD with a higher pCO₂ in winter (JJA) than summer is supported by other observation-based analyses (Yun et al., 2022) and observations with floats (Bushinsky et al., 2019).

In summary, the five models show mixed success in simulating the observation-based SD. The SD in low-to-mid latitudes is relatively well simulated, whereas the simulated SD in the high latitudes differ even in sign in most models from the observation-based estimates, which are also uncertain, especially in the Southern Ocean.

3.2. Local Trends in the pCO₂ Seasonal Cycle Amplitude From 1990 to 2014

The local time trend in SA of the observational or model data (Y_t) is obtained by estimating the slope parameter β in the ordinary least-squares linear regression $Y_t = \alpha + \beta t + \epsilon_t$, where t is the year and ϵ_t are independent normally distributed residuals. A significant (at the 5% level) temporal trend in the observation-based SA is detected for 53% (NIES-FFN) to 82% (CMEMS-FFN) of the area of the grid cells including observation-derived data (Figures 2b–2g). For the models, this fraction ranges between 9% (CESM2) and 19% (CanESM5) in the HIST simulations (non-dotted areas in Figures 2i–2m), but only between 3% and 7% in the HISTNAT simulations with no anthropogenic forcing (Figures 2o–2s). For longer periods, significant slopes are detected over larger areas in simulations HIST (e.g., 18%–27% for 1982–2014), but not in HISTNAT.

For the grid cells with a significant slope, the observation-based SA increases by 0.3–4.0 μatm per decade across the six products (1990–2014; area-weighted mean \pm sdv: CMEMS-FFN: 3.8 ± 6.0 ; CSIR-ML6: 3.2 ± 3.6 ; JENA-MLS: 3.0 ± 8.2 ; JMA-MLR: 3.8 ± 4.5 ; MPI-SOMFFN: 4.0 ± 7.3 ; NIES-FFN: 0.3 ± 3.2 ; note the standard error of the mean slope is two orders of magnitude smaller than the standard deviation and the slopes are significantly different from zero). The mean slopes in SA range between 2.0 and 6.1 μatm per decade across the five models in simulations HIST (ACCESS-ESM1-5: 4.0 ± 4.4 ; CESM2: 2.0 ± 5.1 ; CANESM5: 6.1 ± 4.4 ; IPSL-CM6A-LR: 6.1 ± 6.4 ; NorESM2-LM: 4.0 ± 3.6). The mean slope in SA is between -1.6 and 1.3 μatm per decade for the five models and simulations HISTNAT, considering only cells with a significant model slope. Thus, the model range overlaps with the observational estimate for the simulations HIST with anthropogenic forcing, while only the range for simulations HISTNAT without anthropogenic forcing overlaps with zero.

Large and significant positive trends in SA are observed in the subtropical gyres and the northern subpolar gyres with trends of ~ 10 μatm per decade in many grid cells and products (red in Figures 2a–2g). The observation-based products suggest both positive and negative local trends in SA in the Southern Ocean, but trends are also small and insignificant in many grid cells (dotted areas in Figures 2b–2g) in this sparsely sampled remote region. Trends calculated for these products are generally not significant in most tropical grid cells, however, some exceptions exist. The differences between observational products are often large and the interquartile range exceeds 6 μatm per decade in many grid cells, in particular in the Atlantic subtropical gyre, the tropical and South Pacific, and in the Atlantic sector of the Southern Ocean (Figure S4 in Supporting Information S1). The NIES-FFN product shows smaller trends than the other products (Figure 2g vs. Figures 2b–2f).

In the median, the models capture the observation-derived local trends well under historical forcing (Figure 2; Figures S2 and S4 in Supporting Information S1), though with a considerable model-model spread. Large positive trends are simulated around 40°N and 40°S, similar to the observational data. Trends are generally small in the Southern Ocean (40°S–65°S) and the tropics (10°N–10°S).

Under natural forcing only (simulations HISTNAT), the modeled trends in SA are generally small and statistically insignificant (Figures 2n–2s). The median trend in SA is within ± 2 μatm per decade in the vast majority of grid cells (Figures 2n). This suggests that the trends in SA in simulations HIST are mainly driven by anthropogenic forcing.

3.3. Detection and Attribution of Regional Trends

This section presents statistical detection and attribution testing of trends in mean SA in five regional latitude bands that were previously defined by Landschützer et al. (2018): 65°N–40°N, 40°N–10°N, 10°N–10°S, 10°S–40°S, and 40°S–65°S.

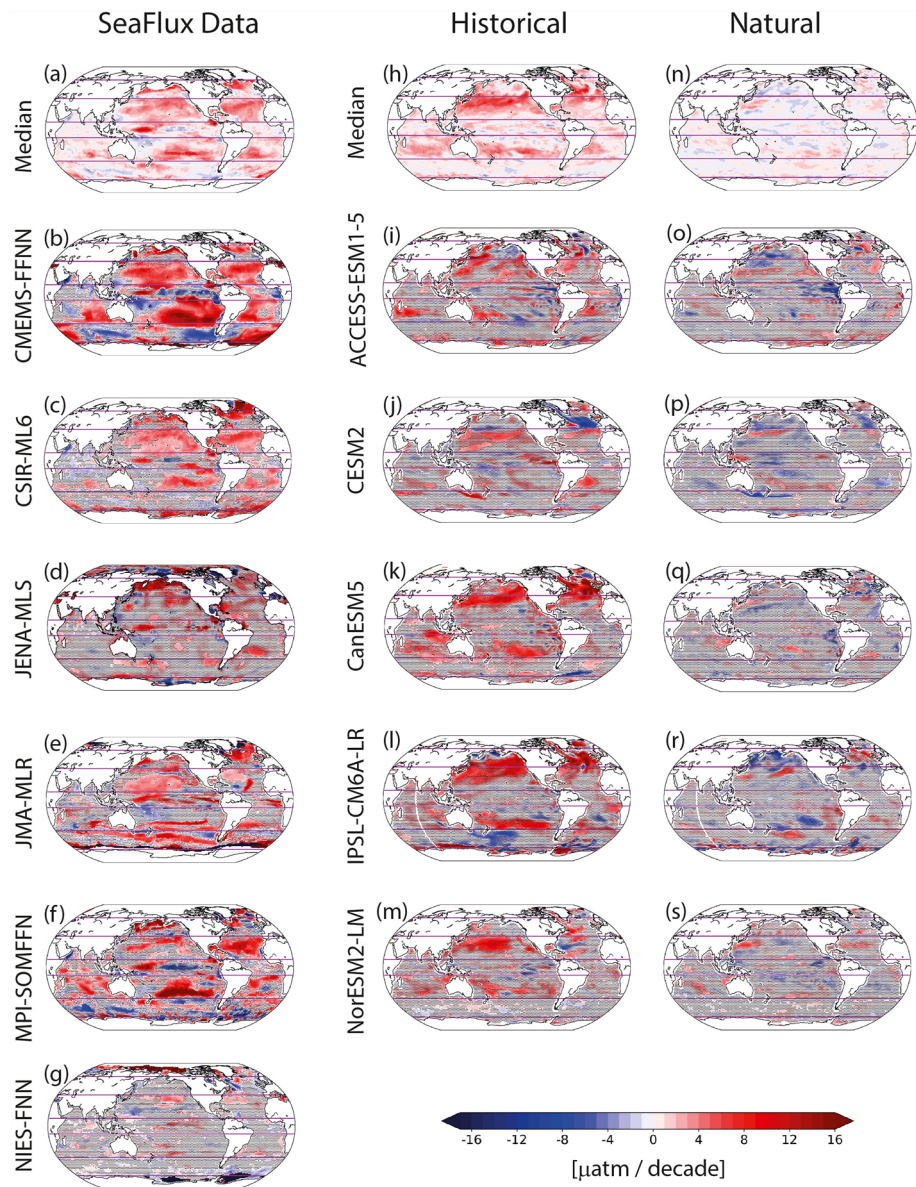


Figure 2. Linear trends in the six-observation-based products (Fay et al., 2021) (a–g) and the CMIP6 climate model simulations of the seasonal amplitude of surface ocean pCO₂ for 1990–2014. The middle panels show results from simulations with anthropogenic and natural forcing (historical, (h)–(m)) and the right panels with natural forcing only (natural, (n)–(s)) for five models, and their median. Slopes are not significant (95% confidence interval) in dotted areas; significance is not indicated for the median results (a, h, n). Results from historical simulations with additional models are shown in Figures S2 and S4 in Supporting Information S1. The seasonal amplitude is the absolute difference between the winter and summer mean ($|DJF - JJA|$).

Rather than fit time trends to each set of model simulations separately, we have used an ANalysis of COVariance (ANCOVA) model to simultaneously fit trends to all the model simulations. This approach has the advantage of giving more precise estimates of the trend slopes, and their uncertainties, because the residual variance is estimated using the data from all the simulations. We assume that the area-weighted, mean seasonal amplitude in a chosen latitude band $Y_{m,s,t}$ in year $t \in [1990, 1991, \dots, 2014]$ from model $m \in [0, 1, 2, 3, 4]$ under scenario $s \in [0, 1]$ (HISTNAT and HIST, respectively) is well represented by the two-way ANCOVA model $Y_{m,s,t} = \alpha_{m,s} + \beta_s t + \epsilon_{m,s,t}$ where $\epsilon_{m,s,t}$ are independent normally distributed residuals with common variance, that is, $\epsilon_{m,s,t} \sim N(0, \sigma^2)$. The model estimates 13 parameters (10 intercepts, 2 slopes, and the variance) using 250 data values (5 models \times 2 scenarios \times 25 years) compared to having to estimate 30 parameters (3 parameters for 5 models \times 2 scenarios) if

linear trends were fit to each model separately. The model was fit to the data easily using Ordinary Least Squares regression $Y \sim m + s + m: s + t + t: s$ with m and s as factors ($m = 0$ and $s = 0$ were aliased to the intercept). We applied a similar ANCOVA model to the observational products to fit the SA of each latitude band $Y_{p,t}$ from product $p \in [0, 1, 2, 3, 4, 5]$ by $Y_{p,t} = \alpha_p + \beta t + \epsilon_{p,t}$. Thus for a region, only one slope is fitted per ensemble (HIST, HISTNAT, observational products).

Figure 3 shows the time series of the SA and trend fits for the five selected zonal bands. The ANCOVA model is reliably fitting the data from the 5 different models ($r^2 > 0.97$; 0.33 in tropics), and so the time trend is scenario rather than model dependent and there is no need to add an interaction term $\beta_{m,s}t$ to the fit. The ANCOVA model fits also well the observational data in the northern high-latitude ($r^2:0.67$) and mid-latitude regions (40°N – 10°N :0.84, 10°S – 40°S :0.89). r^2 is smaller in the tropics (0.17) and Southern Ocean (0.47) as SA and trends are small in these two regions.

Table 1 presents the trend slope parameter estimates and their associated standard errors. Trends are clearly detected in the observational data at the 5% level of significance (as shown by bold face estimates) in latitude bands 65°N – 40°N , 40°N – 10°N , and 10°S – 40°S . There is no significant trend in the equatorial band 10°N – 10°S , and the Southern Ocean (40°S – 65°S). Trends are detected in the same bands in the HIST simulations, and no trends are detected in the HISTNAT simulations - prescribed natural forcing does not cause any long-term trend in SA over the period 1990 to 2014 in the ESM simulations. Individual ESMs simulate similar regional trends in SA (Figures 2 and 3). This is remarkable, in particular, as the ESMs show substantial differences in the spatial patterns of SD (Figure 1) and in the region-averaged magnitude of SA , evident as offsets between the different curves in Figure 3.

Attribution of the trends can be assessed by performing a two-sided hypothesis test on whether or not the observed and simulated slopes are significantly different. Under the null hypothesis of no slope difference, the $T = (\beta_i - \beta_j) / \sqrt{s_{\beta_i}^2 + s_{\beta_j}^2}$ statistic (where s_{β} is the standard error of the β slope estimate) is Student t-distributed with effective degrees of freedom $\nu = (s_i^2 + s_j^2)^2 / (s_i^4/\nu_i + s_j^4/\nu_j)$ (Welch, 1947) where $\nu_i = 25 - 2 = 23$ for the observational products and $\nu_j = 250 - 12 = 238$ for the simulation ANCOVA fits. We assume that the data from the observational products are not independent because they are derived from the same measurements. Values for the t statistic are shown in the table for regions where trends are detected, and are denoted in bold face when the t values are smaller in magnitude than the 0.975 quantile of a t-distribution with ν degrees of freedom.

The observation-based trends in SA in the regions 65°N – 40°N , 40°N – 10°N , and 10°S – 40°S are captured by the HIST but not the HISTNAT simulations, and so can be attributed to anthropogenic forcing. Model results are also consistent with the observed absent trends in the tropics (10°N – 10°S) and the southern high-latitude region (40°S – 65°S).

4. Conclusions

We analyzed trends in the seasonal cycle amplitude of $p\text{CO}_2$ in CMIP6 ESM simulations and six observation-based products for the period 1990 to 2014. We attribute the observed trend in SA in the regions 65°N – 40°N , 40°N – 10°N , and 10°S – 40°S to anthropogenic forcing using an Analysis of Covariance and t -test statistics (Table 1). Simulated and observation-based trends are indistinguishable from zero in 40°S – 65°S and 10°N – 10°S . The trends in the simulations with natural forcing only are indistinguishable from zero in all major regions (Table 1) and in the vast majority of ocean grid cells (Figures 2n–2s).

Uncertainties in the observation-derived trends in SA are high. The interquartile range of the six products exceeds $5 \mu\text{atm/decade}$ in substantial parts of the mid-latitude North Atlantic, the tropical and South Pacific, and the Atlantic sector of the Southern Ocean (Figure S4b in Supporting Information S1). The high uncertainty hampers trend attribution for smaller regions, and we were not able to detect and attribute trends in SA (1990–2014) in the high-latitude (65°N – 40°N) Atlantic and Pacific regions (Figure S5, Table S2 in Supporting Information S1). Deviations between products are not restricted to trends but are surprisingly large for the regionally-averaged, climatological mean SA ; differences are around $10 \mu\text{atm}$ for the mid-latitude and northern North Atlantic regions and $21 \mu\text{atm}$ for the northern North Pacific (offsets of regression lines in Figure 3; Figure S5 in Supporting Information S1).

The data-model comparison reveals large discrepancies in the winter minus summer difference in $p\text{CO}_2$ (SD) in high latitudes, with many models showing an inverse phasing of the seasonal cycle compared to the observational

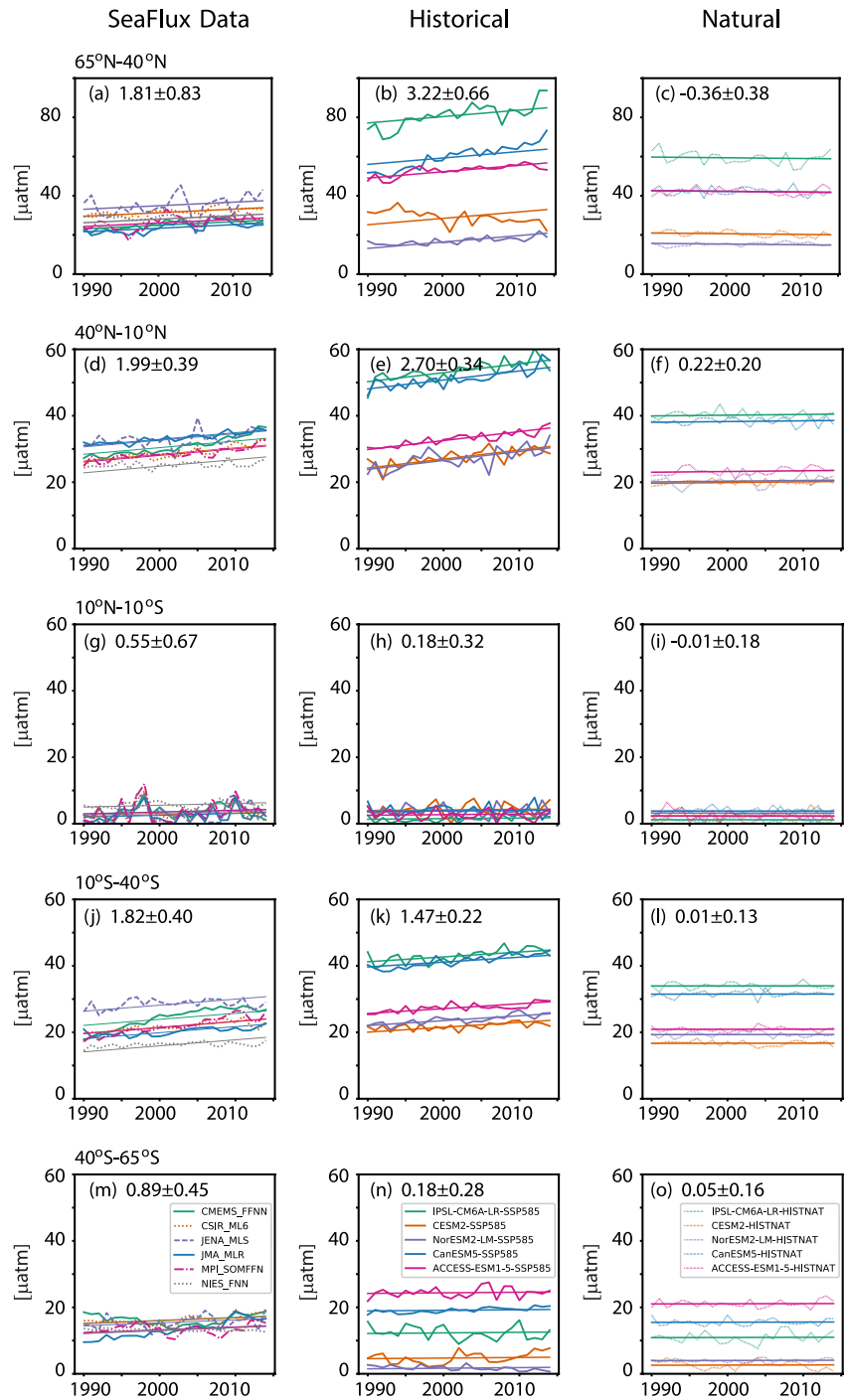


Figure 3. Temporal evolution of the seasonal amplitude in $p\text{CO}_2$. Regional averages are for the ensembles of observational products (left) and simulations with historical (middle) and natural forcing only (right) for 1990–2014. Results from linear regressions are shown by thin solid lines, with identical slope, β , for each ensemble within a region following the ANCOVA model. Numerical values for the slopes β and their standard errors are given in $\mu\text{atm}/\text{decade}$ in each panel and Table 1. Seasonal amplitudes are computed by first averaging the $p\text{CO}_2$ data for each region for 3-monthly periods and then taking the absolute difference between winter and summer values ($|DJF - JJA|$). Note different axis scaling for panels (a) to (c). Results for the northern Pacific and Atlantic (65°N – 40°N) are shown in Figure S5 in Supporting Information S1.

Table 1
Temporal Trends in the Seasonal Cycle Amplitude of pCO₂ and Attribution to Anthropogenic Forcing

Region	Trend: $\beta(s)$ [$\mu\text{atm}/\text{decade}$]			$T(\nu)$ statistics for attribution	
	OBS	HIST	HISTNAT	OBS-HIST	OBS-HISTNAT
65°N–40°N	1.81 (0.83)	3.22 (0.66)	−0.36 (0.38)	−1.34 (47)	2.38 (26)
40°N–10°N	1.99 (0.39)	2.70 (0.34)	0.22 (0.20)	−1.37 (53)	4.01 (28)
10°N–10°S	0.55 (0.67)	0.18 (0.32)	−0.01 (0.18)		
10°S–40°S	1.82 (0.40)	1.47 (0.22)	0.01 (0.13)	0.76 (30)	4.27 (22)
40°S–65°S	0.89 (0.45)	0.18 (0.28)	0.05 (0.16)		

Note. Trends (β) and their standard errors (s , in parentheses) are estimated for five regions and 1990–2014 from data-based products (OBS) (Fay et al., 2021), and from results of five CMIP6 models (Gillett et al., 2016) with prescribed natural (HISTNAT), and natural and anthropogenic forcing (HIST). Trends significantly different from zero are shown in bold (based on a t -test at the 5% level of significance). For regions where trends are significant (detected) in the observations, the difference between simulated and observed trends is quantified using t -statistics (bold if not significant at the 5% level of significance) with effective degrees of freedom ν given in parentheses. Results for the period 1982–2014 and the northern Pacific and Atlantic (65°N–40°N) are given in Tables S1 and S2 in Supporting Information S1.

products (Figure 1; Figure S1 in Supporting Information S1). We also performed the ANCOVA analysis for trends in SD. As expected from the data-model mismatch in the seasonal phasing, the attribution of the trend in SD to anthropogenic forcing fails for 65°N–40°N, while the results are similar for SD and SA for the other four latitude bands (Table S3 in Supporting Information S1, Table 1). Model-model differences are large and the interquartile range around the median SD is exceeding 50 μatm in many regions for the five models discussed in the main text as well as for all 19 CMIP6 models with anthropogenic and natural forcing (Figure S3 in Supporting Information S1). The median and the ensemble spread are similar for the sets of five and 19 models (Figures S3 and S4 in Supporting Information S1), suggesting that the results from the five models are representative of the CMIP6 ensemble. For forced ocean-only model simulations, large model-model and data product-model discrepancies in regional seasonality of the net air-to-sea CO₂ flux have also been identified for northern and southern high-latitudes and the Southern Hemisphere subtropics (Fay & McKinley, 2021). This calls for model improvements, in particular in high-latitude regions, to better represent pCO₂ seasonality. A next step is to identify the drivers for pCO₂ seasonality in models and data to understand these model-data differences. Despite these shortcomings in the mean state, regionally-averaged modeled trends in SA and SD agree with the observation-based trends in four of the five investigated regions (Table 1, Figure S3 in Supporting Information S1, Figure 3) and are firmly attributed to anthropogenic forcing in mid-latitude regions.

Data Availability Statement

Data to reproduce the figures are provided on Zenodo (<https://doi.org/10.5281/zenodo.8081291>). Model output from the DAMIP simulations is distributed through the Earth System Grid (<https://esgf-data.dkrz.de/projects/cmip6-dkrz/>). The SeaFlux surface ocean pCO₂ data (Fay et al., 2021) are available here: <https://doi.org/10.5281/zenodo.5482547>.

References

- Bakker, D. C. E., Pfeil, B., Landa, C. S., Metz, N., O'Brien, K. M., Olsen, A., et al. (2016). A multi-decade record of high-quality fCO₂ data in version 3 of the Surface Ocean CO₂ Atlas (SOCAT). *Earth System Science Data*, 8(2), 383–413. <https://doi.org/10.5194/essd-8-383-2016>
- Barnett, T., Zwiers, F., Henger, G., Allen, M., Crowley, T., Gillett, N., et al. (2005). Detecting and attributing external influences on the climate system: A review of recent advances. *Journal of Climate*, 18(9), 1291–1314. <https://doi.org/10.1175/JCLI3329.1>
- Boucher, O., Servonnat, J., Albright, A. L., Aumont, O., Balkanski, Y., Bastrikov, V., et al. (2020). Presentation and evaluation of the IPSL-CM6A-LR climate model. *Journal of Advances in Modeling Earth Systems*, 12(7), e2019MS002010. <https://doi.org/10.1029/2019MS002010>
- Broecker, W. S., Takahashi, T., Simpson, H. J., & Peng, T. H. (1979). Fate of fossil fuel carbon dioxide and the global carbon budget. *Science*, 206(4417), 409–418. <https://doi.org/10.1126/science.206.4417.409>
- Burger, F. A., John, J. G., & Frölicher, T. L. (2020). Increase in ocean acidity variability and extremes under increasing atmospheric CO₂. *Biogeosciences*, 17(18), 4633–4662. <https://doi.org/10.5194/bg-17-4633-2020>
- Burger, F. A., Terhaar, J., & Frölicher, T. (2022). Compound marine heatwaves and ocean acidity extremes. *Nature Communications*, 12(18), 1–12. <https://doi.org/10.1038/s41467-022-32120-7>
- Bushinsky, S. M., Landschützer, P., Rödenbeck, C., Gray, A. R., Baker, D., Mazloff, M. R., et al. (2019). Reassessing Southern Ocean air-sea CO₂ flux estimates with the addition of biogeochemical float observations. *Global Biogeochemical Cycles*, 33(11), 1370–1388. <https://doi.org/10.1029/2019GB006176>

Acknowledgments

This work was funded by the Swiss National Science Foundation (200020_200511; PP00P2_198897) and the European Union's Horizon 2020 research and innovation program under grant agreement no. 821003 (project 4C, Climate–Carbon Interactions in the Current Century) and no. 820989 (project COMFORT, Our common future ocean in the Earth system-quantifying coupled cycles of carbon, oxygen and nutrients for determining and achieving safe operating spaces with respect to tipping points). The work reflects only the authors' view; the European Commission and their executive agency are not responsible for any use that may be made of the information the work contains. The CSCS Swiss National Supercomputing Center provided computing resources. We thank the CMIP and DAMIP communities for providing simulation results and two reviewers for helpful comments.

- Danabasoglu, G., Lamarque, J.-F., Bacmeister, J., Bailey, D. A., DuVivier, A. K., Edwards, J., et al. (2020). The community Earth system model version 2 (CESM2). *Journal of Advances in Modeling Earth Systems*, *12*(2), e2019MS001916. <https://doi.org/10.1029/2019MS001916>
- Egleston, E. S., Sabine, C. L., & Morel, F. M. M. (2010). Revelle revisited: Buffer factors that quantify the response of ocean chemistry to changes in DIC and alkalinity. *Global Biogeochemical Cycles*, *24*(1), GB1002. <https://doi.org/10.1029/2008GB003407>
- Eyring, V., Bony, S., Meehl, G. A., Senior, C. A., Stevens, B., Stouffer, R. J., & Taylor, K. E. (2016). Overview of the coupled model inter-comparison project phase 6 (CMIP6) experimental design and organization. *Geoscientific Model Development*, *9*(5), 1937–1958. <https://doi.org/10.5194/gmd-9-1937-2016>
- Fassbender, A. J., Rodgers, K. B., Palevsky, H. I., & Sabine, C. L. (2018). Seasonal asymmetry in the evolution of surface ocean pCO₂ and pH thermodynamic drivers and the influence on sea-air CO₂ flux. *Global Biogeochemical Cycles*, *32*(10), 1476–1497. <https://doi.org/10.1029/2017GB005855>
- Fay, A. R., Gregor, L., Landschützer, P., McKinley, G. A., Gruber, N., Gehlen, M., et al. (2021). Seaflux: Harmonization of air–sea CO₂ fluxes from surface pCO₂ data products using a standardized approach. *Earth System Science Data*, *13*(10), 4693–4710. <https://doi.org/10.5194/essd-13-4693-2021>
- Fay, A. R., & McKinley, G. A. (2021). Observed regional fluxes to constrain modeled estimates of the ocean carbon sink. *Geophysical Research Letters*, *48*(20), e2021GL095325. <https://doi.org/10.1029/2021GL095325>
- Friedlingstein, P., O'Sullivan, M., Jones, M. W., Andrew, R. M., Gregor, L., Hauck, J., et al. (2022). Global carbon budget 2022. *Earth System Science Data*, *14*(11), 4811–4900. <https://doi.org/10.5194/essd-14-4811-2022>
- Gallego, M. A., Timmermann, A., Friedrich, T., & Zeebe, R. E. (2018). Drivers of future seasonal cycle changes in oceanic pCO₂. *Biogeosciences*, *15*(17), 5315–5327. <https://doi.org/10.5194/bg-15-5315-2018>
- Gallego, M. A., Timmermann, A., Friedrich, T., & Zeebe, R. E. (2020). Anthropogenic intensification of surface ocean interannual pCO₂ variability. *Geophysical Research Letters*, *47*(13), e2020GL087104. <https://doi.org/10.1029/2020GL087104>
- Gillett, N. P., Kirchmeier-Young, M., Ribes, A., Shiogama, H., Hegerl, G. C., Knutti, R., et al. (2021). Constraining human contributions to observed warming since the pre-industrial period. *Nature Climate Change*, *11*(3), 207–212. <https://doi.org/10.1038/s41558-020-00965-9>
- Gillett, N. P., Shiogama, H., Funke, B., Hegerl, G., Knutti, R., Matthes, K., et al. (2016). The detection and attribution model Intercomparison project (DAMIP v1.0) contribution to CMIP6. *Geoscientific Model Development*, *9*(10), 3685–3697. <https://doi.org/10.5194/gmd-9-3685-2016>
- Gorgues, T., Aumont, O., & Rodgers, K. B. (2010). A mechanistic account of increasing seasonal variations in the rate of ocean uptake of anthropogenic carbon. *Biogeosciences*, *7*(8), 2581–2589. <https://doi.org/10.5194/bg-7-2581-2010>
- Hameau, A., Frölicher, T. L., Mignot, J., & Joos, F. (2020). Is deoxygenation detectable before warming in the thermocline? *Biogeosciences*, *17*(7), 1877–1895. <https://doi.org/10.5194/bg-17-1877-2020>
- Hameau, A., Mignot, J., & Joos, F. (2019). Assessment of time of emergence of anthropogenic deoxygenation and warming: Insights from a CESM simulation from 850 to 2100 CE. *Biogeosciences*, *16*(8), 1755–1780. <https://doi.org/10.5194/bg-16-1755-2019>
- Hauck, J., & Völker, C. (2015). Rising atmospheric CO₂ leads to large impact of biology on Southern Ocean CO₂ uptake via changes of the Revelle factor. *Geophysical Research Letters*, *42*(5), 1459–1464. <https://doi.org/10.1002/2015GL063070>
- Hegerl, G., Hoegh-Guldberg, O., Casassa, G., Hoerling, M. P., Kovats, R., Parmesan, D. W., et al. (2010). Good practice guidance paper on detection and attribution related to anthropogenic climate change. In T. Stocker, et al. (Eds.), *Meeting report of the intergovernmental panel on climate change expert meeting on detection and attribution of anthropogenic climate change* (pp. 1–8). IPCC Working Group I Technical Support Unit, University of Bern, Bern.
- Joos, F., Sarmiento, J., & Siegenthaler, U. (1991). Estimates of the effect of Southern Ocean iron fertilization on atmospheric CO₂ concentrations. *Nature*, *349*(6312), 772–775. <https://doi.org/10.1038/349772a0>
- Keller, K. M., Joos, F., & Raible, C. C. (2014). Time of emergence of trends in ocean biogeochemistry. *Biogeosciences*, *11*(13), 3647–3659. <https://doi.org/10.5194/bg-11-3647-2014>
- Kwiatkowski, L., & Orr, J. (2018). Diverging seasonal extremes for ocean acidification during the twenty-first century. *Nature Climate Change*, *8*(2), 141–145. <https://doi.org/10.1038/s41558-017-0054-0>
- Kwiatkowski, L., Torres, O., Aumont, O., & Orr, J. C. (2022). Modified future diurnal variability of the global surface ocean CO₂ system. *Global Change Biology*, *29*(4), 982–997. <https://doi.org/10.1111/gcb.16514>
- Landschützer, P., Gruber, N., Bakker, D. C. E., Stemmler, I., & Six, K. D. (2018). Strengthening seasonal marine CO₂ variations due to increasing atmospheric CO₂. *Nature Climate Change*, *8*(2), 146–150. <https://doi.org/10.1038/s41558-017-0057-x>
- Lerner, P., Romanou, A., Kelley, M., Romanski, J., Ruedy, R., & Russell, G. (2021). Drivers of air–sea CO₂ flux seasonality and its long-term changes in the NASA–GISS model CMIP6 submission. *Journal of Advances in Modeling Earth Systems*, *13*(2), e2019MS002028. <https://doi.org/10.1029/2019MS002028>
- McNeil, B., & Sasse, T. (2016). Future ocean hypercapnia driven by anthropogenic amplification of the natural CO₂ cycle. *Nature*, *529*(7586), 383–386. <https://doi.org/10.1038/nature16156>
- Revelle, R., & Suess, H. E. (1957). Carbon dioxide exchange between atmosphere and ocean and the question of an increase of atmospheric CO₂ during the past decades. *Tellus*, *9*(1), 18–27. <https://doi.org/10.1111/j.2153-3490.1957.tb01849.x>
- Rodgers, K. B., Sarmiento, J. L., Aumont, O., Crevoisier, C., Montégut, C. d. B., & Metzl, N. (2008). A wintertime uptake window for anthropogenic CO₂ in the North Pacific. *Global Biogeochemical Cycles*, *22*(2), GB2020. <https://doi.org/10.1029/2006GB002920>
- Seland, Ø., Bentsen, M., Seland Graff, L., Olivie, D., Toniazzo, T., Gjermundsen, A., et al. (2020). The Norwegian Earth system model, NorESM2—Evaluation of the CMIP6 DECK and historical simulations. *Geoscientific Model Development Discussions* (pp. 1–68). <https://doi.org/10.5194/gmd-2019-378>
- Swart, N. C., Cole, J. N. S., Kharin, V. V., Lazare, M., Scinocca, J. F., Gillett, N. P., et al. (2019). The Canadian Earth system model version 5 (CanESM5.0.3). *Geoscientific Model Development*, *12*(11), 4823–4873. <https://doi.org/10.5194/gmd-12-4823-2019>
- Welch, B. L. (1947). The generalization of “student’s” problem when several different population variances are involved. *Biometrika*, *34*(1/2), 28–35. <https://doi.org/10.2307/2332510>
- Yun, J., Jeong, S., Gruber, N., Gregor, L., Ho, C.-H., Piao, S., et al. (2022). Enhance seasonal amplitude of atmospheric CO₂ by the changing Southern Ocean carbon sink. *Science Advances*, *8*(41), eabq0220. <https://doi.org/10.1126/sciadv.abq0220>
- Zeebe, R. E., & Wolf-Gladrow, D. (2001). *CO₂ in seawater: Equilibrium, kinetics, isotopes*. Elsevier.
- Ziehn, T., Chamberlain, M. A., Law, R. M., Lenton, A., Bodman, R. W., Dix, M., et al. (2020). The Australian Earth system model: ACCESS-ESM1.5. *Journal of Southern Hemisphere Earth Systems Science*, *70*(1), 193–214. <https://doi.org/10.1071/ES19035>